Materials Today Physics 11 (2019) 100139

Contents lists available at ScienceDirect

Materials Today Physics

journal homepage: https://www.journals.elsevier.com/materials-today-physics

Ultralow thermal conductance of the van der Waals interface between organic nanoribbons

Y. Xiong [a, f], X. Yu [b, c, f], Y. Huang [d], J. Yang [e], L. Li [d], N. Yang [b, c, *], D. Xu [a, **]

[a] Department of Mechanical and Automation Engineering, The Chinese University of Hong Kong, Shatin, New Territories, Hong Kong Special Administrative Region, People's Republic of China
[b] State Key Laboratory of Coal Combustion, Huazhong University of Science and Technology, Wuhan, 430074, People's Republic of China
[c] Nano Interface Center for Energy (NICE), School of Energy and Power Engineering, Huazhong University of Science and Technology, Wuhan 430074, People's Republic of China
[d] State Key Laboratory of New Ceramics and Fine Processing, School of Materials Science and Engineering, Tsinghua University, Beijing 100084, People's Republic of China
[e] School of Mechanical Engineering and Jiangsu Key Laboratory for Design and Manufacture of Micro-Nano Biomedical Instruments, Southeast University, Nanjing, 210096, People's Republic of China

ARTICLE INFO

Article history:
Received 15 August 2019
Received in revised form
17 September 2019
Accepted 18 September 2019
Available online 30 September 2019

Keywords:
Interfacial thermal conductance
Nanoscale van der Waals interface
Copper phthalocyanine nanoribbons
Surface roughness
Stacking configuration

ABSTRACT

Understanding thermal transport through nanoscale van der Waals interfaces is vital for addressing thermal management challenges in nanoelectronic devices such as those made of assembled nanostructure arrays; however, the interfacial thermal conductance (G_{CA}) remains poorly characterized because of technical challenges. In this work, we present an experimental approach and an interface heat transfer model to determine the G_{CA} between two individual copper phthalocyanine (CuPc) nanoribbons. The G_{CA} is found to be on the order of 10^5 $Wm^{-2}K^{-1}$ at 300 K, which is more than two orders of magnitude lower than the value predicted by molecular dynamics (MD) simulations for a perfectly smooth interface between two parallelly aligned CuPc nanoribbons. Further MD simulations and contact mechanics analysis reveal that surface roughness can significantly reduce the adhesion energy and the effective contact area between CuPc nanoribbons and thus result in an ultralow G_{CA}. In addition, the adhesion energy at the interface also depends on the stacking configuration of two CuPc nanoribbons, which also contributes to the observed ultralow G_{CA}. This work provides a new approach for studying thermal transport through nanoscale van der Waals interfaces and discloses the critical role of nanoscale surface roughness in reducing the G_{CA}.

1. Introduction

Nanostructures, such as nanotubes, nanowires, and nanoribbons, are typically assembled into large-area arrays to construct efficient electronic and photonic devices [1,2]. Therefore, a large density of nanoscale van der Waals interfaces exists in those devices. The shrinking size and escalating integration density of transistors impose serious challenges for thermal management of electronic devices, especially for those with high-density interfaces. Understanding thermal transport through nanoscale van der Waals interfaces is crucial for addressing heat dissipation problems in those devices.

Interfacial thermal conductance (G_{CA}) is related to both materials in contact and interface properties including surface roughness, interfacial bonding, and dislocations [3,4]. It has been demonstrated that surface roughness could lead to a significant reduction in interfacial thermal conductance because of the lack of effective contact [3–7]. A few recent studies show that introducing nanostructures at the interface can dramatically enhance interfacial thermal conductance as compared with the flat one [8,9]. The enhanced interfacial thermal conductance is attributed to the enlarged effective contact area because the gaps between nanostructures are filled up by the deposition of metal and thus heat can transport through not only the top and bottom surfaces but also the side walls of the nanostructures. The van der Waals interface between nanostructures is featured with restricted contact area and

* Corresponding author.
** Corresponding author.
E-mail addresses: nuo@hust.edu.cn (N. Yang), dyxu@mae.cuhk.edu.hk (D. Xu).
[f] Y.X. and X.Y. contributed equally to this work.

https://doi.org/10.1016/j.mtphys.2019.100139
2542-5293/

weak interactions. Experimental investigation of thermal transport through nanoscale van der Waals interfaces is very challenging because of technical difficulties in terms of sample preparation and measurement sensitivity. Yang et al. [10] measured the contact thermal resistance between multiwalled carbon nanotubes (MWCNTs) and reported that the G_{CA} is proportional to the nanotube diameter, which is explained by the anisotropic thermal conductivity and long phonon mean free path along the *c*-axis of graphite [10]. Hirotani et al. [11] studied the thermal boundary conductance between one end of a carbon nanotube and an Au surface and showed that the G_{CA} depends on the orientation of anisotropic carbon-based materials. Zhou et al. [12] reported that the G_{CA} of the nanosized contact between an indium arsenide (InAs) nanowire and a silicon nitride (SiN_x) substrate is two orders of magnitude lower than the value predicted by the diffuse mismatch model, which is attributed to the weak adhesion strength of van der Waals interactions. Pettes et al. [13] showed that the contact thermal conductance between a bismuth telluride (Bi_2Te_3) nanoplate and platinum (Pt) electrodes is one to two orders of magnitude lower than the predicted value for an atomically smooth interface. While these studies provide important experimental data for understanding thermal properties of nanoscale van der Waals interfaces, thermal transport through the van der Waals interface between organic nanostructures has rarely been probed.

Recently, metal phthalocyanines, a class of organic semiconductor materials, have attracted much attention because of their advantages of facile synthesis, low-cost availability, tunable properties, and flexibility. Their optical and electrical properties have been extensively studied for applications in organic photovoltaic cells [14,15], light-emitting diodes [16], infrared electroluminescent diodes, and field-effect transistors [17–19]. The low thermal conductivity of organic metal phthalocyanines and the interfacial thermal resistance are of major concerns for heat dissipation in these devices [4,20]. Besides, the stacking structure of planar metal phthalocyanine molecules provides unique opportunities to explore how molecular orientation affects thermal transport through the van der Waals interface.

In this work, we experimentally investigated thermal transport through the van der Waals interface between two individual CuPc nanoribbons. Multiple thermal measurements were carefully carried out on segments cut from the same CuPc nanoribbon to determine the thermal resistance of the contact region of two segments by using a suspended thermal bridge method [21,22]. An interface heat transfer model was developed to extract the G_{CA} between CuPc nanoribbons. Ultralow interfacial thermal conductance on the order of 10^5 $Wm^{-2}K^{-1}$ was observed for the planar contact between CuPc nanoribbons, which is three orders of magnitude lower than the G_{CA} previously reported for the point contact between MWCNTs [12]. Molecular dynamics (MD) simulations and contact mechanics analysis were performed to elucidate fundamental mechanisms for the observed ultralow G_{CA}.

2. Material and methods

2.1. Synthesis of CuPc nanoribbons

As shown in Fig. 1a, a CuPc molecule has a planar structure, which is comprised of a central Cu atom surrounded by four pyrrole rings. A benzene ring is attached to each pyrrole ring. Two neighboring pyrrole rings are connected by an N atom. CuPc molecules form a quasi-one-dimensional molecular column via the π-π interaction, while adjacent columns are bonded with each other by the van der Waals force. Fig. 1a also depicts the herringbone stacking of CuPc molecules for β-phase CuPc.

In this work, CuPc nanoribbons were synthesized via a physical vapor deposition method, as described in our previous study [23]. In brief, CuPc powders (>99.95%; Sigma-Aldrich) were placed at the high-temperature zone of a horizontal three-zone tube furnace and vaporized at 450 °C for an hour. The vapor was carried by high-purity argon gas at a rate of 200 sccm from the high-temperature zone to the low-temperature zone. Single-crystalline CuPc nanoribbons were formed on a silicon substrate placed at the low-temperature zone (200–300 °C). CuPc nanoribbons we synthesized are β-phase with a growth direction of [010]. The synthesized CuPc nanoribbons were kept under vacuum to prevent the contamination from the ambient environment.

2.2. Thermal resistance measurements

In this work, thermal resistances of CuPc nanoribbons were measured by using a thermal bridge method [21,22]. As shown in Fig. 2a, the measurement device consists of two suspended membranes. Serpentine Pt coils were patterned on the membranes, acting as heat source and heat sink in the thermal measurement, respectively. All the measurements were performed under a high vacuum with a pressure less than 10^{-6} torr in a cryostat system (Janis CCS-400H/204) to minimize convective heat loss and surface contamination. The suspended length and the width of the CuPc nanoribbons were determined by scanning electron microscopy (SEM), and the thickness was measured by atomic force microscopy (AFM).

To exclude the variation among samples, a uniform CuPc nanoribbon was cut into five segments using an in-house-built micromanipulator. For each sample, e.g., sample C1, two segments were transferred onto a measurement device to form a planar contact, as shown in Fig. S1d. Other three segments were also transferred onto measurement devices, bridging two membranes with three different suspended lengths (Fig. S1a-c). The intrinsic thermal conductivity of the CuPc nanoribbon and the contact thermal resistance between the CuPc nanoribbon and two membranes can be extracted from the measured thermal resistances of three single CuPc nanoribbons. Then, the thermal resistance of the contact region between two CuPc nanoribbons can be determined. More details are given in the Supplementary Material. After the measurement, each sample was characterized by SEM, which confirms that the interface between two nanoribbons is very clean.

2.3. MD simulations

MD simulations were performed using a large-scale atomic/molecular massively parallel simulator (LAMMPS) package. Class II force field potential forms including high-order functions, and cross terms were applied to describe interatomic interactions including structural components (bonds, angles, and dihedrals) and non-bonding interactions (Lennard-Jones and electrostatic interactions). All the potential parameters were taken from the study by Shao et al. [24]. A cutoff distance of 10 Å was used for both the Lennard-Jones and electrostatic potentials. The detailed calculation of the electrostatic potential and the Lennard-Jones potential can be found in the Supplementary Material. Boundaries along *a*, *b*, and *c* axes were set to be free, fixed, and free, respectively. A time step of 0.5 fs was chosen owing to fast vibrating hydrogen atoms. The details of the LAMMPS package for CuPc nanoribbons are listed in Table S1 in the Supplementary Material.

3. Results and discussion

The crystalline structure of CuPc nanoribbons was characterized by high-resolution atomic force microscopy (HRAFM). The HRAFM

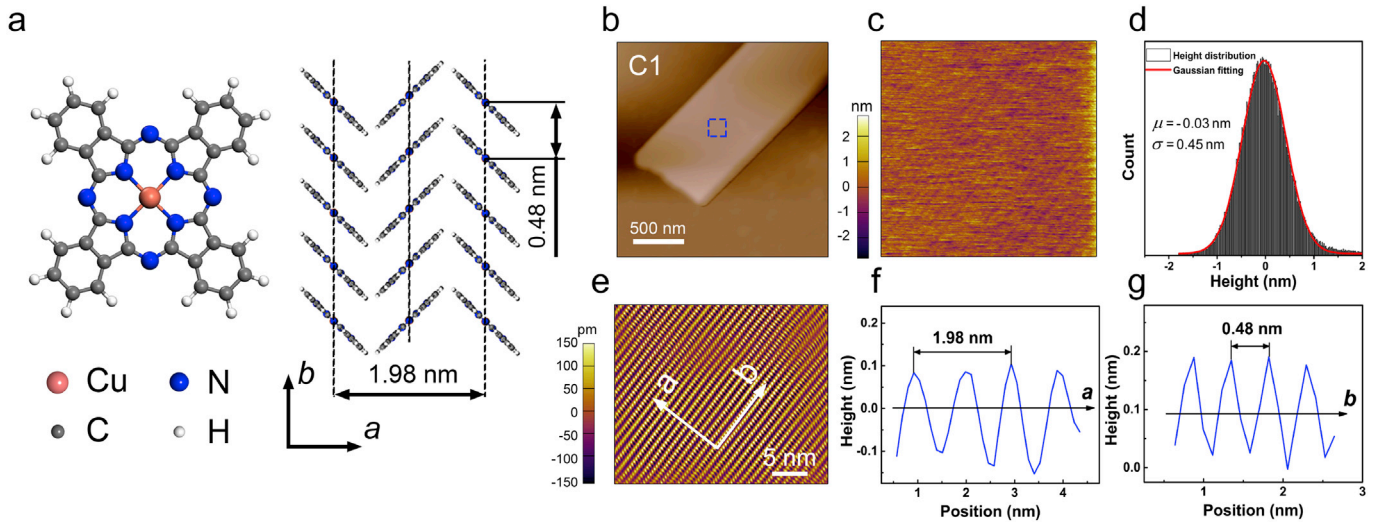

Fig. 1. Molecular structure and AFM characterization of CuPc nanoribbons. (a) Schematics of the planar CuPc molecule and the herringbone stacking of CuPc molecules for β-phase CuPc. (b) AFM image of one measured CuPc nanoribbon sample (C1). The blue dash square indicates where HRAFM was taken. (c) HRAFM image of sample C1 processed with flattening and plane fitting routines. The scan size is 30 nm × 30 nm. (d) The surface height histogram for the image in (c) and the Gaussian fitting curve. (e) HRAFM image of sample C1 processed with flattening, plane fitting, and Fourier transform. (f, g) Surface scanning profiles for the *a*-axis and the *b*-axis. The lattice constants determined for the *a*-axis and the *b*-axis are 1.98 nm and 0.48 nm, respectively, confirming that CuPc nanoribbons studied in this work are β-phase. AFM, atomic force microscopy; HRAFM, high-resolution atomic force microscopy.

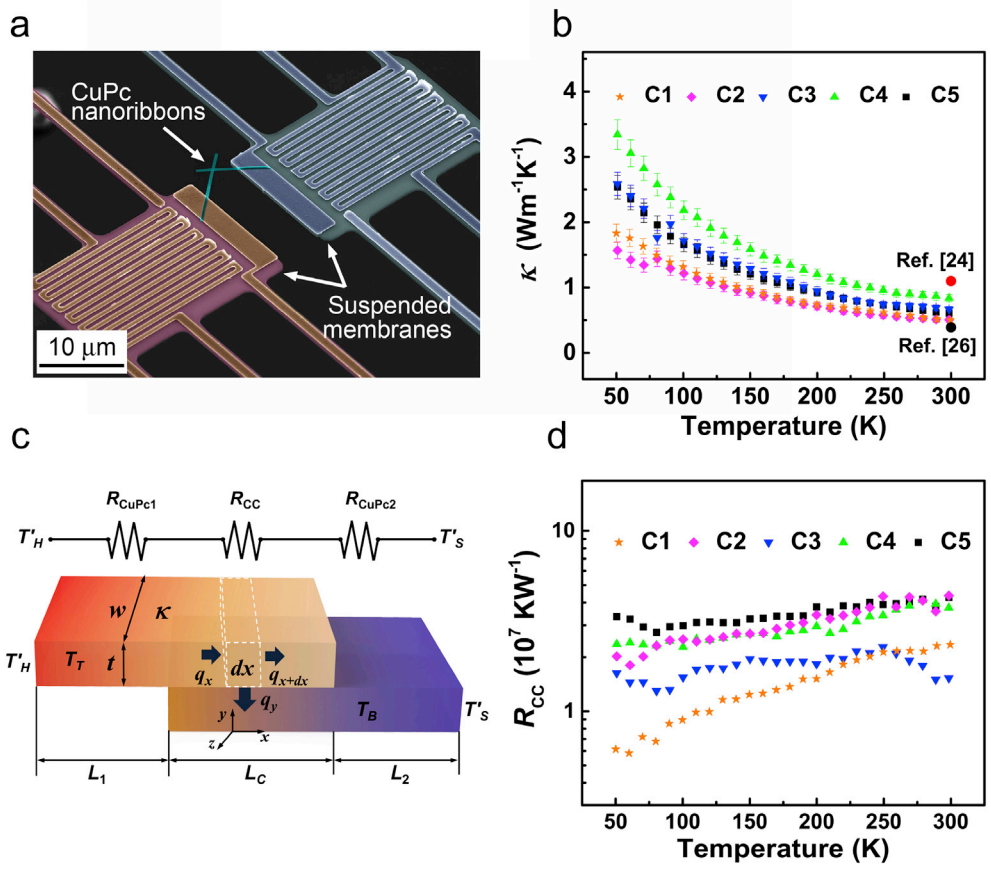

Fig. 2. (a) False-color SEM micrograph of two CuPc nanoribbons with a planar contact on a suspended device for thermal measurement. (b) Extracted intrinsic thermal conductivity (κ) for five samples (C1–C5). The extracted thermal conductivity of CuPc nanoribbons ranges from 0.50 to 0.86 $Wm^{-1}K^{-1}$ at 300 K, which is comparable with the experimental and MD results previously reported in the literature [24,26]. (c) Schematic of two nanoribbons in contact with an overlap length L_C used for deriving the interface heat transfer model and the corresponding thermal circuit. (d) Experimentally determined R_{CC} for five samples (C1–C5). MD, molecular dynamics; SEM, scanning electron microscopy.

image of one measured CuPc nanoribbon sample (C1) is given in Fig. 1e, which clearly shows the crystalline orientation. The lattice constants determined from surface scanning profiles (Fig. 1f and g) are 1.98 nm and 0.48 nm for the *a*-axis and the *b*-axis, respectively, confirming that CuPc nanoribbons studied in this work are β-phase [25].

Fig. 2a shows two CuPc nanoribbons with a planar contact, bridging the suspended membranes of the measurement device. To extract the G_{CA} between CuPc nanoribbons, the thermal resistance of the contact region between two CuPc nanoribbons (R_{CC}) was first determined by conducting multiple thermal measurements on segments from the same CuPc nanoribbon. Fig. 2b shows the extracted intrinsic thermal conductivity (κ) for five samples (C1–C5). Jin et al. [26] measured the room-temperature thermal conductivity of crystalline CuPc thin films using the 3ω method and reported a value of 0.39 $Wm^{-1}K^{-1}$. MD simulations conducted by Shao et al. [24] reported a thermal conductivity value of 1.1 $Wm^{-1}K^{-1}$ for crystalline CuPc. The extracted thermal conductivity of CuPc nanoribbons ranges from 0.50 to 0.86 $Wm^{-1}K^{-1}$ at 300 K, which is comparable with the experimental and MD results reported in the literature [24,26]. Fig. 2d plots the obtained R_{CC} as a function of temperature for five samples (C1–C5). The R_{CC} varies among samples, and the values are on the order of 10^7 KW^{-1}.

For heat conduction through an interface between two quasi-one-dimensional nanostructures, heat flows along the nanostructure horizontally but through the interface vertically. To determine the G_{CA}, some approximations were commonly made by researchers [27–30]. For example, Zhong and Lukes [28] performed MD simulations on the interfacial thermal resistance between parallelly aligned carbon nanotubes with an overlap region. In their study, the interfacial thermal resistance was calculated by simplifying the overlap region as a planar interface between two coaxial nanotubes joined end to end [28]. In the work of Yang et al. [30], the thermal resistance of the overlap region of two MWCNTs was treated as a contact thermal resistor connected in series with two MWCNT thermal resistors with the half of the overlap length. In these studies, thermal resistances of CNTs are relatively small compared with the interfacial thermal resistance, and thus, the aforementioned approximations might be reasonable. However, for thermal transport through the planar contact between CuPc nanoribbons with low thermal conductivity, an interface heat transfer model should be considered in the contact region to extract the G_{CA}.

An analytical model was developed in this work, which assumes one-dimensional heat conduction in each nanoribbon and constant G_{CA} for the interface between two nanoribbons. Fig. 2c illustrates a schematic of two parallelly aligned nanoribbons with an overlap length L_C. Heat flows along each nanoribbon in the horizontal direction and through the interface in the vertical direction, as indicated by arrows in Fig. 2c. Two nanoribbons are assumed to have the same width (w), thickness (t), and thermal conductivity (κ) because they are cut from the same CuPc nanoribbon. The steady-state heat diffusion equations for top and bottom nanoribbons in the contact region can be written as

$$\kappa \frac{d^2T_T}{dx^2} wtdx - G_{CA}(T_T - T_B)wdx = 0 \tag{1a}$$

$$\kappa \frac{d^2T_B}{dx^2} wtdx + G_{CA}(T_T - T_B)wdx = 0 \tag{1b}$$

where T_T and T_B denote the temperatures of top and bottom nanoribbons, respectively. The details of the interface heat transfer model can be found in the Supplementary Material. The model we derived is similar to the two-temperature model [31–34] and the two-channel thermal transport model [35]. Note that all the heat will be conducted through the interface between two nanoribbons; heat rate (q) can be calculated by integrating the heat flux over the interface and can be derived as

$$q = \frac{\gamma\kappa wt\left(e^{\gamma L_C} - 1\right)\left(T'_H - T'_S\right)}{1 + e^{\gamma L_C} + \gamma\left(e^{\gamma L_C} - 1\right)(L_1 + L_2 + L_C/2)} \tag{2}$$

where $\gamma = \sqrt{2G_{CA}/\kappa t}$, T'_H is the temperature at the joint of the top nanoribbon and the heating membrane, and T'_S is the temperature at the joint of the bottom nanoribbon and the sensing membrane. Thus, R_{CC} can be derived as

$$R_{CC} = \frac{T_T|_{-L_C/2} - T_B|_{L_C/2}}{q} = \frac{L_C}{2\kappa wt} + \frac{\gamma L_C\left(e^{\gamma L_C} + 1\right)}{2\left(e^{\gamma L_C} - 1\right)} \frac{1}{wL_C G_{CA}} \tag{3}$$

the G_{CA} can be determined from the experimentally measured R_{CC} by solving Eq. (3).

The calculated temperature profiles of both top and bottom nanoribbons in the contact region clearly deviate from the linear distribution for the segments in the non-contact region for sample C1 (Fig. S3). In the work of Yang et al., the thermal resistance of the overlap region of two MWCNTs was treated as a contact thermal resistor connected in series with two MWCNT thermal resistors with the half of the overlap length [30]. By adopting this approximation approach, the thermal resistance of the contact region can be expressed as

$$R_{CC,\,app} = \frac{L_C}{\kappa wt} + \frac{1}{wL_C G_{CA}} \tag{4}$$

Compared with the analytical model we derived, the approximation approach overestimates the first term at the right hand side of Eq. (3) by a factor of 2, which leads to overestimation of G_{CA} for

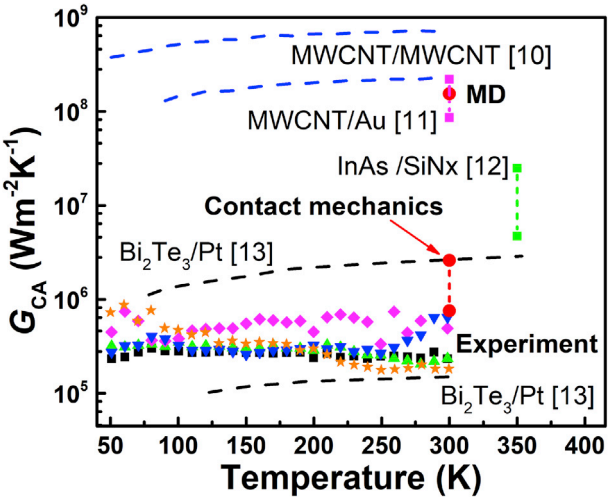

Fig. 3. Experimentally determined G_{CA} for the van der Waals interface between CuPc nanoribbons. The G_{CA} determined by the MD simulation for the interface between two perfectly smooth CuPc nanoribbons is 1.54×10^8 $Wm^{-2}K^{-1}$ (red dot). The G_{CA} between two rough CuPc nanoribbons estimated by combining MD simulations and contact mechanics analysis is 2.6×10^6 $Wm^{-2}K^{-1}$ and 7.55×10^5 $Wm^{-2}K^{-1}$ (red dash line), respectively, corresponding to the mean separation distances proposed in the studies by Rumpf [43] and Rabinovich et al. [44]. The G_{CA} results reported for other van der Waals interfaces in the literature are also shown for comparison. MD, molecular dynamics; MWCNT, multiwalled carbon nanotube.

CuPc nanoribbons with relatively large intrinsic thermal resistances.

The extracted G_{CA} is shown in Fig. 3 for five measured samples (C1–C5). At room temperature, the values of G_{CA} range from 1.8×10^5 to 6.5×10^5 $Wm^{-2}K^{-1}$. The relative uncertainty in $G_{CA}$is estimated to be in the range of 48%–120% for five samples (C1–C5). The detailed uncertainty analysis is given in the Supplementary Material. The G_{CA} we obtained for the van der Waals interface between CuPc nanoribbons is two to three orders of magnitude lower than the values for typical phonon-dominated interfaces [36–38]. The G_{CA} results reported in the literature for other nanoscale van der Waals interfaces are also shown in Fig. 3 for comparison. Yang et al. [10] reported a G_{CA} on the order of 10^8 $Wm^{-2}K^{-1}$ for the point contact between MWCNTs, as shown by blue dash lines in Fig. 3. The G_{CA} between one end of an MWCNT and an Au surface is determined to be 8.6×10^7–2.2×10^8 $Wm^{-2}K^{-1}$ (pink dash line) [11]. Zhou et al. [12] reported that the G_{CA} between an InAs nanowire and a SiN_x substrate is 4.7×10^6–2.5×10^7 $Wm^{-2}K^{-1}$ (green dash line). The contact thermal resistance per unit area for the interface between a Bi_2Te_3 nanoplate and Pt electrodes is in the range of 2.8×10^{-7}–1×10^{-5} m^2KW^{-1}, corresponding to a G_{CA} of 1×10^5–3.5×10^6 $Wm^{-2}K^{-1}$ (black dash line) [13]. Compared with these studies, the G_{CA} we obtained for the planar contact between CuPc nanoribbons is one to three orders of magnitude lower than the G_{CA} values reported for the interfaces of MWCNT/MWCNT [10], MWCNT/Au [11], and InAs nanowire/SiN_x [12] but very close to the results for the interface of Bi_2Te_3 nanoplate/Pt [13].

To elucidate the underlying mechanisms responsible for the observed ultralow G_{CA}, we performed atomistic MD simulations on thermal transport through the interface between CuPc nanoribbons. The inset of Fig. 4 depicts the MD simulation system of two parallelly aligned CuPc nanoribbons forming a planar contact. The equilibrium distance between two CuPc nanoribbons is about 0.4 nm, which is close to the interlayer spacing in the *c*-axis of β-phase CuPc. The non-equilibrium MD method was applied to calculate the temperature profiles of top and bottom CuPc nanoribbons, and the results are fitted fairly well by using the analytical model we derived, as shown in Fig. 4. The G_{CA} determined by the MD simulation is 1.54×10^8 $Wm^{-2}K^{-1}$, which is denoted by a red dot in Fig. 3. This value is comparable with the simulation result previously reported for van der Waals interfaces [39] but more than two orders of magnitude higher than our experimental values (1.8–6.5×10^5 $Wm^{-2}K^{-1}$).

It is worth noting that the surfaces of CuPc nanoribbons are assumed to be perfectly smooth in the MD simulation; however, the samples we measured always have a certain level of surface roughness. The surface roughness of CuPc nanoribbons was characterized by using a contact mode AFM (AR Cypher, Oxford, UK). The scan size is 30 nm × 30 nm with 256 pixels for each axis. Fig. 1c shows the AFM image of sample C1 processed with flattening and plane fitting routines. Fig. 1d plots the surface height histogram corresponding to the image in Fig. 1c, which can be fitted well by using a Gaussian distribution with a mean height of −0.03 nm and a root-mean-square (rms) roughness (σ) of 0.45 nm. Because the contact between two rough surfaces occurs only at peaks, the spacing between two surfaces varies from point to point, which will affect the adhesion energy and thus the G_{CA} between two surfaces. However, it is very difficult to determine the G_{CA} for the interface between two rough CuPc nanoribbons through MD simulations. Instead, we calculated the average adhesion energy between two rough CuPc surfaces by combining MD simulations and contact mechanics analysis. To do so, we first calculated the adhesion energy between two perfectly smooth CuPc nanoribbons (E) by MD simulations when one ribbon is fixed and the other one is gradually moved away from the equilibrium position (the displacement or the separation distance is denoted as s), as shown by the green solid line in Fig. 5. The adhesion energy reaches the maximum value of 0.12 Jm^{-2} (E_0) at the equilibrium position ($s = 0$), which is a typical value for van der Waals interfaces [40]. The calculated E decreases with s quickly and approaches zero when s is larger than 8 Å. In contact mechanics, it is well accepted that the contact between two elastic rough surfaces with an rms roughness of σ can be modeled as the contact between a flat elastic surface and a rigid rough surface with an rms roughness of $\sqrt{2}\sigma$ [41]. We followed the same approach in this work and treated two rough CuPc nanoribbons as a flat elastic surface and an equivalent rigid rough surface in contact. The mean separation distance between two contacting surfaces depends on material properties, surface profiles, and external load. At a given separation distance, the average adhesion energy ($\bar{E}$) can

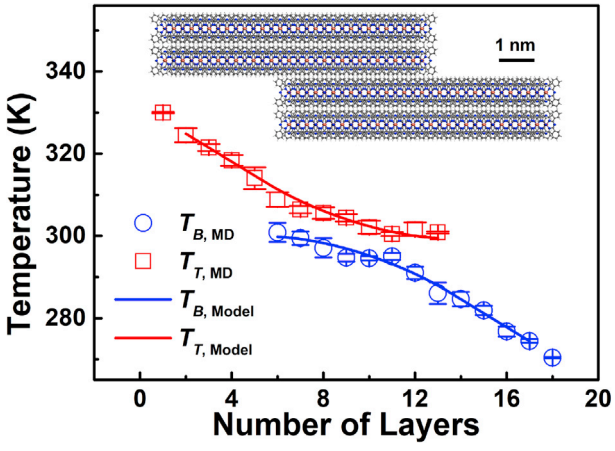

Fig. 4. Temperature profiles of top and bottom nanoribbons calculated by the MD simulation (symbols) and the fitting curves by using the interface heat transfer model (solid lines). The inset shows the MD simulation system of two parallelly aligned CuPc nanoribbons forming a planar contact. The molecular stacking at the interface is identical to the packing inside the CuPc nanoribbon (pristine stacking). MD, molecular dynamics.

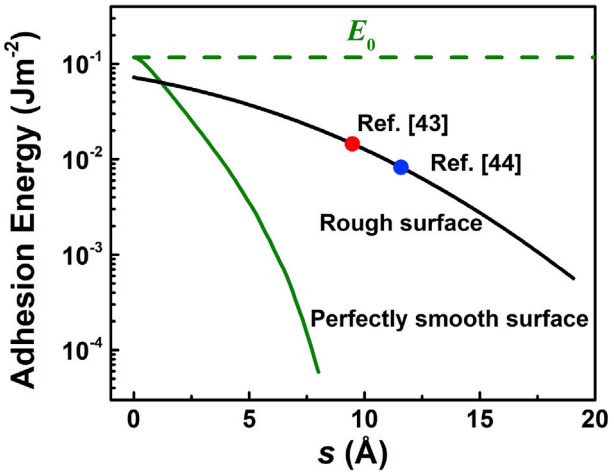

Fig. 5. Adhesion energies calculated for perfectly smooth (green solid line) and rough CuPc nanoribbons (black solid line) as a function of the separation distance. The green dash line shows the adhesion energy for two perfectly smooth CuPc nanoribbons at the equilibrium position ($s = 0$) as the reference. Red and blue dots denote average adhesion energies estimated for the interface between two rough CuPc nanoribbons by using the mean separation distances proposed in the studies by Rumpf [43] and Rabinovich et al. [44], respectively.

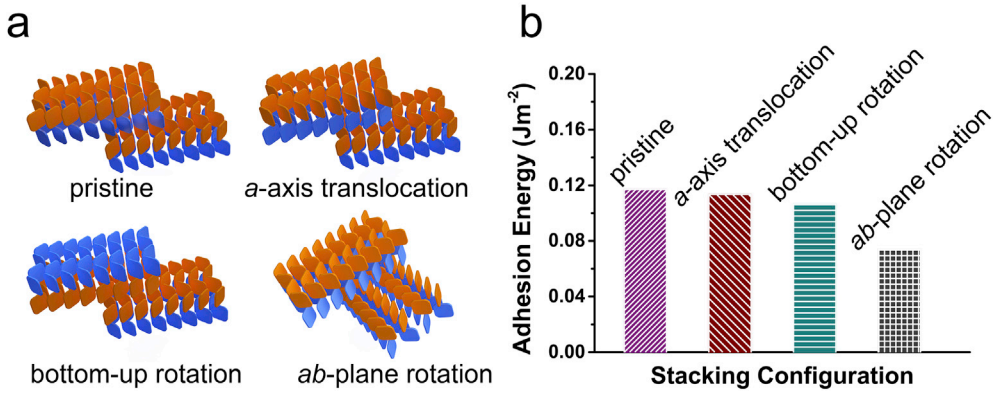

Fig. 6. Effect of stacking configurations on the adhesion energy between CuPc nanoribbons. (a) Schematics of four stacking configurations. (d) Adhesion energies calculated for different stacking configurations by MD simulations. MD, molecular dynamics.

be calculated based on the variation of E with s for two perfectly smooth surfaces (green solid line in Fig. 5) and the Gaussian distribution of surface heights for the equivalent rough surface. In the calculation, for the peaks with a surface height larger than the given separation distance, the corresponding adhesion energy is assumed to be E_0, which is similar to Maugis' approximation [42]. The variation of the calculated average adhesion energy with the mean separation distance is shown as the black solid line in Fig. 5. Notably, when the equivalent rough surface is squeezed onto the flat surface and mean planes of two surfaces are overlapped ($s = 0$), the average adhesion energy is 0.065 Jm^{-2}, only 55% of the adhesion energy between two perfectly smooth CuPc nanoribbons. In our experiments, no external force is applied onto two CuPc nanoribbons, so the mean separation distance should be larger than zero. In the literature, simple approaches have been proposed to estimate the mean separation distance between two surfaces from surface roughness. For example, Rumpf [43] suggested to take the mean separation distance as 1.485 times of the rms surface roughness for the contact between a smooth particle and a rough surface. This gives a mean separation distance of 0.95 nm and a $\overline{E}/E_0$ of 13%, as indicated by the red dot in Fig. 5. Rabinovich et al. [44] suggested that the mean separation distance could be approximated by 1.817 times of the rms surface roughness, corresponding to a $\overline{E}/E_0$ of 7% (blue dot in Fig. 5). According to Prasher's model [7], the G_{CA} is proportional to the square of the surface adhesion strength (or the adhesion energy). Thus, by using the mean separation distances proposed by Rumpf [43] and Rabinovich et al. [44], the G_{CA} between two rough CuPc nanoribbons can be estimated from the MD result for two perfectly smooth CuPc nanoribbons and is equal to 2.6×10^6 $Wm^{-2}K^{-1}$ and 7.55×10^5 $Wm^{-2}K^{-1}$ (red dash line in Fig. 3), respectively, which are close to our experimental results.

This analysis shows that surface roughness will lead to an increase of the mean separation distance between two CuPc nanoribbons. As a result, the adhesion energy and the G_{CA} between two rough CuPc nanoribbons could be substantially lower than the counterparts for two perfectly smooth CuPc nanoribbons in the MD simulation. The contact between two rough CuPc nanoribbons may be reexamined in terms of the effective contact area by taking adhesion into account. Owing to their elastic nature, adhesion will occur for two contacting CuPc nanoribbons. At molecular scale, the van der Waals interaction pulls two surfaces into contact, which will decay quickly with the increase of the distance. When two CuPc nanoribbons form a planar contact, a certain portion of surfaces is too far away from each other to sustain the adequate adhesion because of the surface roughness. The real contact area of an adhesive contact strongly depends on adhesion strength, material properties, and roughness parameters [45,46]. Surface roughness is taken into account through the dimensionless rms slope $h' \equiv \langle |\nabla h|^2 \rangle^{1/2}$, where h is the height profile of the rough surface. h' is estimated to be 0.63 for CuPc nanoribbons according to the AFM image (Fig. 1c). Recently, Persson and Scarraggi [45] showed that the relative contact area A/A_0 is around 0.06 at zero external load for surfaces with adhesion energy of 0.1 Jm^{-2}, rms roughness of 0.6 nm, and $h'$of 0.0035. CuPc nanoribbons measured in this work have adhesion energy (0.12 Jm^{-2}) and rms roughness (0.45 nm) similar to those of the surface studied in the work by Persson and Scarraggi [45] but much larger h' (0.63). It should be noted that surface heights can only be measured at discrete points by AFM and that experimental noise becomes a critical issue at small scan sizes. Indeed, experimental results of h' could vary over a wide range depending on the measurement technique and the scan size. It is still under debate how to measure h' accurately [47,48]. Instead of pursuing its precise value, we intend to discuss the role of h' in determining A/A_0 for adhesive contacts. CuPc nanoribbons synthesized via the physical vapor deposition method possess highly crystalline structure and rather clean surfaces, as evidenced by AFM and SEM. We expect that h' will be smaller than the estimated value (0.63). McGhee et al. [49] experimentally showed that A/A_0 decreases with the increase of h'. Therefore, A/A_0 for CuPc nanoribbons is expected to be smaller than the value (0.06) predicted by Persson and Scaraggi [45]. Considering the effective contact area, the G_{CA} between two rough CuPc nanoribbons is estimated to be lower than 9.24×10^6 $Wm^{-2}K^{-1}$. It can be concluded that surface roughness could result in a significantly reduced effective contact area and thus a much lower G_{CA}. A recent study [50] indicates that the contact between nanoribbons may be improved by wetting the van der Waals interface.

It should be noted that there are several possible stacking configurations for two CuPc nanoribbons. Considering that molecular stacking may affect the adhesion between two contacting surfaces [51,52], we calculated adhesion energies for different stacking configurations of two CuPc nanoribbons using MD simulations. Fig. 6a enumerates four stacking configurations: pristine stacking, a-axis translocation, bottom-up rotation, and ab-plane rotation. In the pristine stacking, the atomic arrangement at the interface is identical to the packing inside a CuPc nanoribbon. On the basis of the pristine stacking, one ribbon is turned upside down in the bottom-up rotation configuration. In the a-axis translocation, CuPc molecules in one nanoribbon are slid by half of the lattice constant along the a-axis, while one nanoribbon is rotated by 90° for the ab-plane rotation. As seen in Fig. 6b, the pristine stacking

demonstrates the highest adhesion energy (0.12 Jm^{-2}) among four stacking configurations, while the adhesion energy of the *ab*-plane rotation is only 0.07 Jm^{-2}, corresponding to 58% of the pristine stacking. In view of the fact that the stacking configuration of CuPc nanoribbons in our experiments (Fig. 2a) is similar to the *ab*-plane rotation, the lower adhesion energy of this configuration may also contribute to the observed ultralow G_{CA}.

Furthermore, some other surface phenomena such as surface reconstruction might occur in nanostructures [53]. Previous studies suggested that surface reconstruction could decrease surface energies of Si, Ge, and Au [54–56]. Compared with Si or Au nanomaterials, CuPc nanoribbons should have a much lower surface energy because of weak intermolecular interactions. In addition, as seen from the HRAFM image (Fig. 1e), the surface of CuPc nanoribbons exhibits very good lattice ordering. Therefore, we expect surface reconstruction is negligible for CuPc nanoribbons.

4. Conclusions

This work sheds light on understanding thermal transport through the van der Waals interface between nanostructures. Distinct from the point contact between MWCNTs, surface roughness plays a pronounced role for thermal transport through the planar contact between CuPc nanoribbons. MD simulations and contact mechanics analysis reveal that surface roughness will significantly reduce the adhesion energy and the effective contact area between CuPc nanoribbons, which will result in orders of magnitude lower G_{CA}. This explains the ultralow G_{CA} observed for CuPc nanoribbons as well as other planar contact [13]. In addition, our MD simulations disclose that the adhesion energy at the interface depends on the stacking configuration, which may also contribute to the observed ultralow G_{CA}.

Acknowledgements

D.X. acknowledges the funding support from the Research Grants Council of the Hong Kong Special Administrative Region, People's Republic of China, under the General Research Fund (RGC Ref. No. 14238416). N.Y. acknowledges the funding support from National Natural Science Foundation of China (Grant No. 51576076 and No. 51711540031), Natural Science Foundation of Hubei Province (Grant No. 2017CFA046), and Fundamental Research Funds for the Central Universities (HUST: Grant No. 2016YXZD006). J.Y. acknowledges the funding support from the National Natural Science Foundation of China (Grant No. 51676036). L.L. acknowledges the funding support from the National Natural Science Foundation of China (Grant No. 51572149). X.Y. and N.Y. acknowledge the National Supercomputing Center in Tianjin (TianHe-1 (A)) and China Scientific Computing Grid (ScGrid) for providing assistance in computations.

Appendix A. Supplementary data

Supplementary data to this article can be found online at https://doi.org/10.1016/j.mtphys.2019.100139.

References

[1] X. Duan, C. Niu, V. Sahi, J. Chen, J.W. Parce, S. Empedocles, J.L. Goldman, High-performance thin-film transistors using semiconductor nanowires and nanoribbons, Nature 425 (2003) 274–278.
[2] R. Yan, D. Gargas, P. Yang, Nanowire photonics, Nat. Photonics 3 (2009) 569–576.
[3] P.E. Hopkins, Thermal Transport across Solid Interfaces with Nanoscale Imperfections: Effects of Roughness, Disorder, Dislocations, and Bonding on Thermal Boundary Conductance, ISRN Mechanical Engineering, 2013, p. 682586.
[4] D.G. Cahill, P.V. Braun, G. Chen, D.R. Clarke, S. Fan, K.E. Goodson, P. Keblinski, W.P. King, G.D. Mahan, A. Majumdar, H.J. Maris, S.R. Phillpot, E. Pop, L. Shi, Nanoscale thermal transport. II. 2003-2012, Appl. Phys. Rev. 1 (2014), 011305.
[5] Z.Y. Ong, E. Pop, Molecular dynamics simulation of thermal boundary conductance between carbon nanotubes and SiO_2, Phys. Rev. B 81 (2010) 155408.
[6] L. Zhang, P. Keblinski, J.S. Wang, B. Li, Interfacial thermal transport in atomic junctions, Phys. Rev. B 83 (2011), 064303.
[7] R. Prasher, Acoustic mismatch model for thermal contact resistance of van der Waals contacts, Appl. Phys. Lett. 94 (2009), 041905.
[8] E. Lee, T. Zhang, T. Yoo, Z. Guo, T. Luo, Nanostructures significantly enhance thermal transport across solid interfaces, ACS Appl. Mater. Interfaces 8 (2016) 35505, 51.
[9] E. Lee, E. Menumerov, R.A. Hughes, S. Neretina, T. Luo, Low-cost nanostructures from nanoparticle-assisted large-scale lithography significantly enhance thermal energy transport across solid interfaces, ACS Appl. Mater. Interfaces 10 (2018) 34690, 40.
[10] J. Yang, M. Shen, Y. Yang, W.J. Evans, Z. Wei, W. Chen, A.A. Zinn, Y. Chen, R. Prasher, T.T. Xu, P. Keblinski, D. Li, Phonon transport through point contacts between graphitic nanomaterials, Phys. Rev. Lett. 112 (2014) 205901.
[11] J. Hirotani, T. Ikuta, T. Nishiyama, K. Takahashi, Thermal boundary resistance between the end of an individual carbon nanotube and a Au surface, Nanotechnology 22 (2011) 315702.
[12] F. Zhou, A. Persson, L. Samuelson, H. Linke, L. Shi, Thermal resistance of a nanoscale point contact to an indium arsenide nanowire, Appl. Phys. Lett. 99 (2011), 063110.
[13] M.T. Pettes, J. Maassen, I. Jo, M.S. Lundstrom, L. Shi, Effects of surface band bending and scattering on thermoelectric transport in suspended bismuth telluride nanoplates, Nano Lett. 13 (2013) 5316–5322.
[14] F. Yang, M. Shtein, S.R. Forrest, Controlled growth of a molecular bulk heterojunction photovoltaic cell, Nat. Mater. 4 (2005) 37–41.
[15] P. Peumans, S. Uchida, S.R. Forrest, Efficient bulk heterojunction photovoltaic cells using small-molecular-weight organic thin films, Nature 425 (2003) 158–162.
[16] P.C. Kao, S.Y. Chu, Z.X. You, S.J. Liou, C.A. Chuang, Improved efficiency of organic light-emitting diodes using CoPc buffer layer, Thin Solid Films 498 (2006) 249–253.
[17] H. Wang, D. Yan, Organic heterostructures in organic field-effect transistors, NPG Asia Mater. 2 (2010) 69–78.
[18] J. Wang, H. Wang, X. Yan, H. Huang, D. Jin, J. Shi, Y. Tang, D. Yan, Heterojunction ambipolar organic transistors fabricated by a two-step vacuum-deposition process, Adv. Funct. Mater. 16 (2006) 824–830.
[19] Q. Tang, H. Li, Y. Song, W. Xu, W. Hu, L. Jiang, Y. Liu, X. Wang, D. Zhu, In situ patterning of organic single-crystalline nanoribbons on a SiO_2 surface for the fabrication of various architectures and high-quality transistors, Adv. Mater. 18 (2006) 3010–3014.
[20] A.L. Moore, L. Shi, Emerging challenges and materials for thermal management of electronics, Mater. Today 17 (2014) 163–174.
[21] L. Shi, D. Li, C. Yu, W. Jang, D. Kim, Z. Yao, P. Kim, A. Majumdar, Measuring thermal and thermoelectric properties of one-dimensional nanostructures using a microfabricated device, J. Heat Transfer 125 (5) (2003) 881–888.
[22] H. Tang, X. Wang, Y. Xiong, Y. Zhao, Y. Zhang, Y. Zhang, J. Yang, D. Xu, Thermoelectric characterization of individual bismuth selenide topological insulator nanoribbons, Nanoscale 7 (2015) 6683–6690.
[23] H. Tang, Y. Xiong, F. Zu, Y. Zhao, X. Wang, Q. Fu, J. Jie, J. Yang, D. Xu, Length-dependent thermal transport in one-dimensional self-assembly of planar π-conjugated molecules, Nanoscale 8 (2016) 11932–11939.
[24] C. Shao, Y. Jin, K. Pipe, M. Shtein, J. Kieffer, Simulation of crystalline and amorphous copper phthalocyanine: force field development and analysis of thermal transport mechanisms, J. Phys. Chem. C 118 (2014) 9861–9870.
[25] C.J. Brown, Crystal structure of β-copper phthalocyanine, J. Chem. Soc. A 10 (1968) 2488–2492.
[26] Y. Jin, C. Shao, J. Kieffer, K.P. Pipe, M. Shtein, Origins of thermal boundary conductance of interfaces involving organic semiconductors, J. Appl. Phys. 112 (2012), 093503.
[27] T. Feng, W. Yao, Z. Wang, J. Shi, C. Li, B. Cao, X. Ruan, Spectral analysis of nonequilibrium molecular dynamics: spectral phonon temperature and local nonequilibrium in thin films and across interfaces, Phys. Rev. B 95 (2017) 195202.
[28] H. Zhong, J.R. Lukes, Interfacial thermal resistance between carbon nanotubes: molecular dynamics simulations and analytical thermal modeling, Phys. Rev. B 74 (2006) 125403.
[29] Z. Zhang, Y. Xie, Q. Peng, Y. Chen, Thermal transport in MoS_2/Graphene hybrid nanosheets, Nanotechnology 26 (2015) 37402.
[30] J. Yang, S. Waltermire, Y. Chen, A.A. Zinn, T.T. Xu, D. Li, Contact thermal resistance between individual multiwall carbon nanotubes, Appl. Phys. Lett. 96 (2010), 023109.
[31] M. An, Q. Song, X. Yu, H. Meng, D. Ma, R. Li, Z. Jin, B. Huang, N. Yang, Generalized two-temperature model for coupled phonons in nanosized graphene, Nano Lett. 17 (2017) 5805–5810.
[32] B. Liao, J. Zhou, G. Chen, Generalized two-temperature model for coupled phonon-magnon diffusion, Phys. Rev. Lett. 113 (2014), 025902.
[33] P. Jiang, X. Qian, X. Gu, R. Yang, Probing anisotropic thermal conductivity of transition metal dichalcogenides MX_2 (M = Mo, W and X = S, Se) using time-domain thermoreflectance, Adv. Math. 29 (2017) 1701068.

[34] Y. Wang, X. Ruan, A.K. Roy, Two-temperature nonequilibrium molecular dynamics simulation of thermal transport across metal-nonmetal interfaces, Phys. Rev. B 85 (2012) 205311.
[35] R.B. Wilson, J.P. Feser, G.T. Hohensee, D.G. Cahill, Two-channel model for nonequilibrium thermal transport in pump-probe experiments, Phys. Rev. B 88 (2013) 144305.
[36] R.M. Costescu, M.A. Wall, D.G. Cahill, Thermal conductance of epitaxial interfaces, Phys. Rev. B 67 (2003), 054302.
[37] H.K. Lyeo, D.G. Cahill, Thermal conductance of interfaces between highly dissimilar materials, Phys. Rev. B 73 (2006) 144301.
[38] P.E. Hopkins, J.C. Duda, S.P. Clark, C.P. Hains, T.J. Rotter, L.M. Phinney, G. Balakrishnan, Effect of dislocation density on thermal boundary conductance across GaSb/GaAs interfaces, Appl. Phys. Lett. 98 (2011) 161913.
[39] F. Sun, T. Zhang, M.M. Jobbins, Z. Guo, X. Zhang, Z. Zheng, D. Tang, S. Ptasinska, T. Luo, Molecular bridge enables anomalous enhancement in thermal transport across hard-soft material interfaces, Adv. Mater. 26 (2014) 6093–6099.
[40] T. Tong, Y. Zhao, L. Delzeit, A. Kashani, M. Meyyappan, A. Majumdar, Height independent compressive modulus of vertically aligned carbon nanotube arrays, Nano Lett. 8 (2008) 511–515.
[41] J.A. Greenwood, J.H. Tripp, The contact of two nominally flat rough surfaces, Proc. Inst. Mech. Eng. 185 (1970) 625–633.
[42] D. Maugis, On the contact and adhesion of rough surfaces, J. Adhes. Sci. Technol. 10 (1996) 161–175.
[43] H. Rumpf, Particle Technology, Springer Science & Business Media, 2012.
[44] Y.I. Rabinovich, J.J. Adler, A. Ata, R.K. Singh, B.M. Moudgil, Adhesion between nanoscale rough surfaces - I. Role of asperity geometry, J. Colloid Interface Sci. 232 (2000) 10–16.
[45] B.N.J. Persson, M. Scaraggi, Theory of adhesion: role of surface roughness, J. Chem. Phys. 141 (2014) 124701.
[46] L. Pastewka, M.O. Robbins, Contact between rough surfaces and a criterion for macroscopic adhesion, Proc. Natl. Acad. Sci. U.S.A. 111 (2014) 3298–3303.
[47] A. Gujrati, S.R. Khanal, L. Pastewka, T.D.B. Jacobs, Combining TEM, AFM, and profilometry for quantitative topography characterization across all scales, ACS Appl. Mater. Interfaces 10 (2018) 29169–29178.
[48] T.D.B. Jacobs, T. Junge, L. Pastewka, Quantitative characterization of surface topography using spectral analysis, Surf Topogr-Metrol. 5 (2017), 013001.
[49] A.J. McGhee, A.A. Pitenis, A.I. Bennett, K.L. Harris, K.D. Schulze, J.M. Uruena, P.G. Ifju, T.E. Angelini, M.H. Muser, W.G. Sawyer, Contact and deformation of randomly rough surfaces with varying root-mean-square gradient, Tribol. Lett. 65 (2017) 157.
[50] J. Yang, Y. Yang, S.W. Waltermire, X. Wu, H. Zhang, T. Gutu, Y. Jiang, Y. Chen, A.A. Zinn, R. Prasher, T.T. Xu, D. Li, Enhanced and switchable nanoscale thermal conduction due to van der Waals interfaces, Nat. Nanotechnol. 7 (2012) 91–95, 2.
[51] J. Wang, X. Mu, X. Wang, N. Wang, F. Ma, W. Liang, M. Sun, The thermal and thermoelectric properties of in-plane C-BN hybrid structures and graphene/h-BN van der Waals heterostructures, Mater. Today Phys. 5 (2018) 29–57.
[52] D. Xu, R. Hanus, Y. Xiao, S. Wang, G.J. Snyder, Q. Hao, Thermal boundary resistance correlated with strain energy in individual Si film-wafer twist boundaries, Mater. Today Phys. 6 (2018) 53–59.
[53] F. Ercolessi, E. Tosatti, M. Parrinello, Au (100) surface reconstruction, Phys. Rev. Lett. 57 (1986) 719–722.
[54] B.W. Dodson, Simulation of Au(100) reconstruction by use of the embedded-atom method, Phys. Rev. B 35 (1987) 880–882.
[55] A.A. Stekolnikov, J. Furthmuller, F. Bechstedt, Absolute surface energies of group-IV semiconductors: dependence on orientation and reconstruction, Phys. Rev. B 65 (2002) 115318.
[56] A.P. Bartok, S. De, C. Poelking, N. Bernstein, J.R. Kermode, G. Csanyi, M. Ceriotti, Machine learning unifies the modeling of materials and molecules, Sci. Adv. 3 (2017) e1701816.